In-vivo assessment of a rat rectal tumor using optical-resolution photoacoustic endoscopy

RIQIANG LIN,[1,2,†] SHENGMIAO LV,[1,3,†] WENJING LOU,[4] XIATIAN WANG,[1,3] ZHIHUA XIE,[1,3] SILUE ZENG,[1] RUI CHEN,[1] WEN GAO,[1] TIANAN JIANG,[4] KA-WAI ERIC CHENG,[2] KWOK-HO LAM,[2,5,6] AND XIAOJING GONG[1,3,7] [ID]

[1]*Research Center for Biomedical Optics and Molecular Imaging, Key Laboratory of Biomedical Imaging Science and System, Shenzhen Institute of Advanced Technology, Chinese Academy of Science, Shenzhen 518055, China*
[2]*Department of Electrical and Electronic Engineering, The Hong Kong Polytechnic University, Hung Hom, Kowloon, Hong Kong, SAR, China*
[3]*Shenzhen Key Laboratory for Molecular Imaging, Guangdong Provincial Key Laboratory of Biomedical Optical Imaging Technology, CAS Key Laboratory of Health Informatics, Shenzhen Institute of Advanced Technology, Chinese Academy of Science, Shenzhen 518055, China*
[4]*Department of Ultrasound Medicine, The First Affiliated Hospital, Zhejiang University School of Medicine, Hangzhou, Zhejiang, China*
[5]*Centre for Medical and Industrial Ultrasonics, James Watt School of Engineering, University of Glasgow, Glasgow, Scotland, United Kingdom*
[6]*kwokho.lam@glasgow.ac.uk*
[7]*xj.gong@siat.ac.cn*
[†]Equal contribution

Abstract: Optical-resolution photoacoustic endoscopy (OR-PAE) has been proven to realize imaging on the vascular network in the gastrointestinal (GI) tract with high sensitivity and spatial resolution, providing morphological information. Various photoacoustic endoscopic catheters were developed to improve the resolution and adaptivity of *in-vivo* imaging. However, this technology has not yet been validated on *in-vivo* GI tumors, which generally feature angiogenesis. The tumor causes thickened mucosa and neoplasia, requiring large depth-of-field (DOF) in imaging, which contradicts to high-resolution imaging. In this work, a novel catheter was developed with a high resolution of ∼27 μm, providing a matched DOF of ∼400 μm to cover the vessels up to the submucosa layer. Optical-resolution photoacoustic endoscopic imaging was first performed on *in-vivo* rat rectal tumors. In addition, to further characterize the vessel morphology, tumor-suspected regions and normal regions were selected for quantification and analysis of vessel dimension distribution and tortuosity. All the results suggest that the OR-PAE has great application potential in tumor diagnosis, evaluation, and monitoring of therapeutic efficacy.

© 2024 Optica Publishing Group under the terms of the Optica Open Access Publishing Agreement

1. Introduction

Endoscopy is an effective measure [1] for early detection and treatment guidance on gastrointestinal (GI) tumors, which can improve the five-year survival rate of patients obviously [2]. The current clinical endoscopic methods, such as white-light imaging and narrow-band imaging, are capable of visualizing internal superficial tissue with high resolution. Amongst, endoscopic ultrasound (EUS) can provide highly accurate assessments of tumor infiltration in depth [3]. Nevertheless, these methods cannot provide the depth-resolved image of vessel network, which is associated with tumor angiogenesis that is highly correlated to the growth and metastasis [4]. The visualization and analysis of angiogenesis characteristics are significant for tumor diagnosis at the early stage.

However, the micron-size neovascular is under the mucosa and has low blood flow speed, which could be a challenge to visualize using the current imaging tools even the Doppler EUS.

Optical-resolution photoacoustic endoscopy (OR-PAE) is a novel imaging tool capable of imaging the vascular network in the GI tract with high sensitivity and spatial resolution. Various designs of miniature OR-PAE catheters were developed for GI imaging. Yang et al. reported the first OR-PAE imaging on an *in-vivo* rat colorectum in 2015 [5], which acquired a three-dimensional vasculature image with a high resolution of 9.2 μm, although the PA imaging holds an incomplete field-of-view of 270 degrees with a blind area of 90 degrees. Besides, the catheter has a long rigid length (~40 mm) and a large outer diameter (~3.8 mm), which is too bulky to pass through the biopsy channels of clinical GI endoscopies. Since then, a number of novel OR-PAE catheters have been developed to overcome challenges for *in-vivo* imaging. Yang et al. reported a series of OR-PAE catheters [6–11] to adapt the irregular GI tract imaging with the 360° field of view. Chen et al. utilized an optomechanical design to realize the focus adjustment in a flexible miniature OR-PAE probe [12]. Xi et al. presented a high-speed OR-PAE probe based on a microelectromechanical systems (MEMS) scanning mirror [13]. The previous efforts focused on the imaging capability of catheters with good adaptability and high imaging speed. Recently, Yang et al. presented an OR-PAE system with a 3.38-mm diameter catheter [14], conducting the GI imaging via the instrument channel of a clinical video endoscope, which boosted the clinical translation of OR-PAE.

The aforementioned work of OR-PAE focused on obtaining the vascular network of healthy GI tracts. For diseased GI tracts, especially with the tumors, *in-vivo* imaging is challenging due to the much-complicated environment induced by tumor. For example, the tumor causes intima swelling and hyperplasia. The thickened mucosa and irregular shape require a matched imaging depth of field (DOF), which is a trade-off against high-resolution imaging. Besides, it is worthwhile to explore a basis for tumor analysis and diagnosis based on the quantification of OR-PAE images with high resolution and large data volume. To overcome these challenges, the OR-PAE should be evaluated in a kind of experimental model on the tumor study of GI tract.

In this work, the vascular network of animal rectums with tumor models was acquired *in vivo* using an OR-PAE catheter developed with a lateral resolution of ~27 μm and a DOF of ~400 μm. The PA images of rat rectal vasculature were successfully acquired, segmented, and quantitatively analyzed. The results show different distribution characteristics of vessels between normal and abnormal regions. The abnormal region presented more micro vessels (<95 μm) and higher tortuosity. All the results are verified by the pathological analysis.

2. Materials and method

2.1. Animal: modeling and imaging

Sprague Dawley (SD) rats (Harlan) were prepared for animal modeling. N-methyl-N-nitrosourea (MNU) [15] and dimethylhydrazine (DMH) [16] are well-known carcinogens for inducing rectal cancer in rats. To accelerate the experimental progress, both drugs were applied to the rats.

MNU was dissolved in sterile distilled water at a concentration of 4 mg/mL. The MNU enema was administered at a dose of 20 mg/kg body weight [17]. The DMH was diluted with physiological saline to 1% solution, which pH was adjusted to 7.0 with a 4% NaOH solution. The DMH solution was injected subcutaneously in the rat neck region at a dose of 30 mg/kg body weight [18].

The animal preparation lasted about four months. The six-week-old SD rats (~200 g) were used in the modeling. The modeling operation was conducted once a week. Fasting is not required prior to drug delivery. Administration continued for about two months until the onset of thin feces, watery diarrhea, and the weight loss was observed, at which point it was ceased. The rats were fasted overnight before the experiment to reduce the likelihood of residual excreta. Before imaging, the rats were anesthetized by applying a mixture of isoflurane and oxygen (2%

isoflurane concentration) at a flow rate of 300 mL/min. Deionized water was injected into the rectum as the acoustic coupling medium.

At the early stage of modeling, the diameter of the rat rectum was only ∼3 mm. A 2.5 mm-diameter polyethylene tube was applied as a protective tube, adapting the rectum size of the young SD rat. The imaging catheter was inserted with the protective tube filled with water to conduct PA and ultrasound imaging. More detailed information on the imaging operation can be found in our previous work [19].

All animal experiments, including the modeling and imaging, were performed in compliance with guidelines and protocols approved by the Animal Study Committee of Shenzhen Institutes of Advanced Technology, Chinese Academy of Sciences.

2.2. OR-PAE platform: catheter and system

The OR-PAE catheter was fabricated as displayed in Figs. 1(a) and (b). A single-mode fiber (core diameter: 9.2 μm, SMF28, Thorlabs, USA) was used to deliver the laser beam. The laser from the fiber was collimated by a gradient-index (GRIN) lens (diameter: 0.5 mm, length: 1.15 mm, 64515, Edmund Optics, USA) and then reflected onto the rectum wall surface by a custom-designed prism (Fuzhou OYeah Optronics Co., Ltd, Fujian, China) with an angle of 32°. A customized coil (Tu's Chengfa Precision Spring Co., Ltd, Guangdong, China) was applied to rotate the imaging probe. The focused laser beam was ∼18.5 μm with a focus length adjusted to 1.5 mm between the catheter and the target (see Supplement 1). The DOF was designed to be >400 μm. The optical simulation was conducted by ZEMAX software. The optical-acoustic overlapped area was from 1 mm to 2 mm radially from the center of the catheter, which covers the rectal mucosa. A 3D-printed base was used for assembling the optical and acoustic elements. A miniature 40-MHz unfocused ultrasound transducer (Blatek, USA) with a dimension of 0.6 mm × 0.5 mm × 0.2 mm and a bandwidth of 40% were sequentially aligned with the prism at the tip of the base.
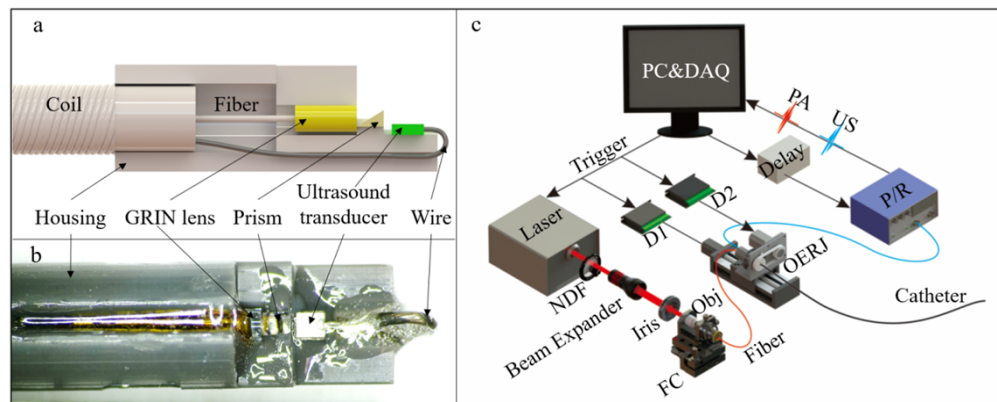
Fig. 1. Schematic and photograph of catheter and OR-PAE system. (a)Schematic of catheter. (b)Photograph of catheter. (c)System setup. DAQ: data acquisition; P/R: pulser/receiver; D: driver; OERJ: optical-electric rotary joint; NDF: neutral density filter; Obj: objective; FC: fiber coupler.

The schematic of the OR-PAE system is presented in Fig. 1(c). The catheter was continually rotated with an optical-electric rotary joint (Shenzhen CENO Electronics Technology Co., Ltd, China), which was driven by a step motor. The pulsed laser (MIL Medical Technology (Shenzhen) Co., Ltd, Shenzhen, China) emitted light at a wavelength of 532 nm, featuring a pulse width of 10 ns and a repeated frequency of 10 kHz, offering an energy output of 1.6 μJ on the tissue.

Thus, the imaging scanning was performed at a rate of 6.25 frames per second, and each B-scan had 1600 A-lines. To perform 3D scanning, a pull-back motorized stage was applied to acquire images at each pull-back with a step size of 20 μm and a moving speed of 125 μm/s. All the signals were transmitted to the pulser-receiver (5073, Olympus, Japan), amplified (39 dB) and then sent to a DAQ (9325, Alarza, Canada) with a sampling rate of 250 MHz/s. The setup of OR-PAE system was similar to our previous work. More detailed information on the system and data acquisition can be found in the published work [19].

The lateral resolution of the OR-PAE is ~27 μm by testing a ~10 μm-diameter tungsten wire. The experimental method and results are described in Supplement 1.

2.3. Quantification method

To investigate whether the rectal vasculature could be identified between normal and tumor region, quantification was conducted to characterize the distribution of vessel based on PA images of rat rectal vasculature.

Once abnormal vasculatures were found in the images, the regions with the area of 4.5 mm × 4.5 mm were chosen as the tumor-suspected regions. Two normal regions near the tumor-suspected region with the continuous vessel networks were selected. The data was quantified using the 3D segmentation and quantification method, which was reported in our previous work [20]. The steps were as follows: the chosen areas were further segmented based on the intensity and structure, respectively. The morphological reconstruction was then conducted based on fusing the two aforementioned segmentation images. The vessel images were enhanced and extracted from the reconstructed images, containing the vessel boundary data. Based on the enhanced images, vessel skeleton was extracted by the Multi-Stencils Fast Marching (MSFM) methods [21]. The vascular profile in the cross-section was represented by a circle, which was fit using the boundary and skeleton data. The quantification results of vascular diameter and tortuosity [22] were then obtained using the below equations [20,21]:

$$Ratio\ of\ diameter = \frac{Number\ of\ all\ small\ vessels\ (<95\ \mu m)}{Number\ of\ all\ vessels} \tag{1}$$

$$Totuosity = Sum\ of\ angles\ metric\ (SOAM) \tag{2}$$

3. Results

3.1. OR-PAE on normal rat rectum in vivo

To demonstrate the imaging capability of the system, OR-PA imaging was performed on a 2-month-old SD rat (~300 g). The catheter was inserted into a normal rat rectum of ~4 cm away from the anus. Figure 2(a) presents the unfolded PA image of a vascular network from the rat rectum. The depth encoded color indicates the relative depth of vessels from the signal detector, in which most vessels are distributed from 1.3 mm to 1.7 mm. The shadow at the top and bottom is the folded tissue in the rectum. Figures 2(b) and (c) are the B-scan images at the position of blue dash Line A, while Figs. 2(d) and (e) are the B-scan images at the position of blue dash Line B in Fig. 2(a). The blue squares mark the enlarged area in Figs. 2(b) and (d), which verified that the DOF was ~400 μm in Figs. 2(c) and (e), respectively.

3.2. OR-PAE on tumor of rat rectum in vivo

An animal modeling experiment was conducted to further investigate the imaging capability of OR-PAE in tumor research. Figure 3 presents the results acquired from three different rat rectums. Figures 3(a), (d) and (g) are the PA images of vessel networks. Some tumor-suspected regions were labeled by blue dashed boxes, which featured micro vessels with high density. To compare the characteristics of labeled regions, the adjacent regions were labeled by white dashed boxes in
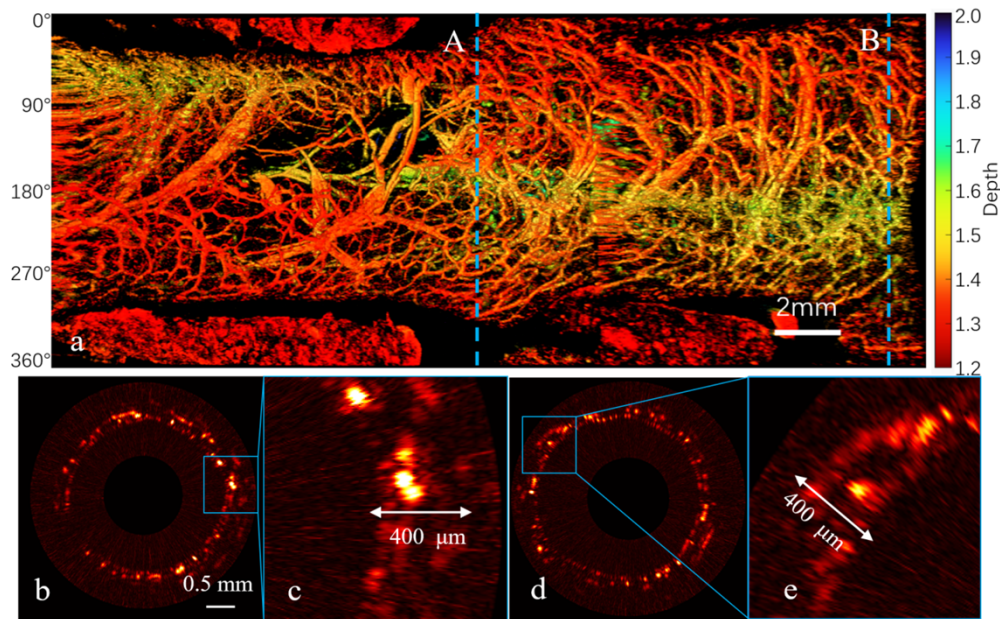
Fig. 2. *In vivo* PA image of normal rat rectum. (a) Depth encoded maximum amplitude projection (MAP); (b) B-scan image and (c) the enlarged images of a blue square at blue dotted Line A; (d) B-scan image and (e) the enlarged images of a blue square at blue dotted Line B.
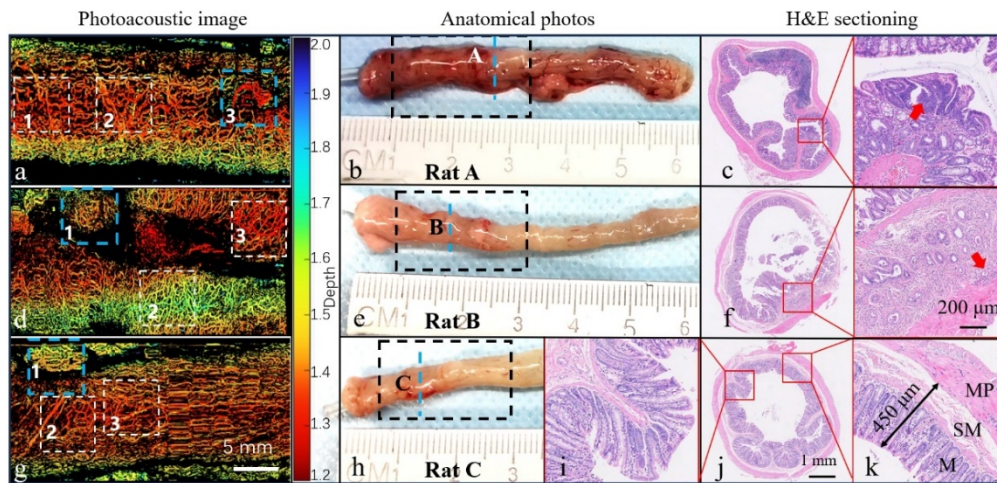
Fig. 3. PA images and anatomical photos of three rat rectums. (a, d, g) Unfolded PA imaging of micro vessels of rat rectums. (b, e, h) Anatomical photos of rat rectums. (c, f, i, j, k) Pathological results. (c) Pathological sectioning at blue dotted Line A; (f) Pathological sectioning at blue dotted Line B (i) Folded structure of the rectal mucosa; (j) Pathological sectioning at blue dotted Line C. White dashed boxes label the normal region; black dashed boxed label the imaging region; blue dotted lines indicate the position of pathological section; red squares show the enlarged regions; red arrows in the enlarged figures indicate the tumor cells. M: mucosa; SM: submucosa; MP: muscularis propria.
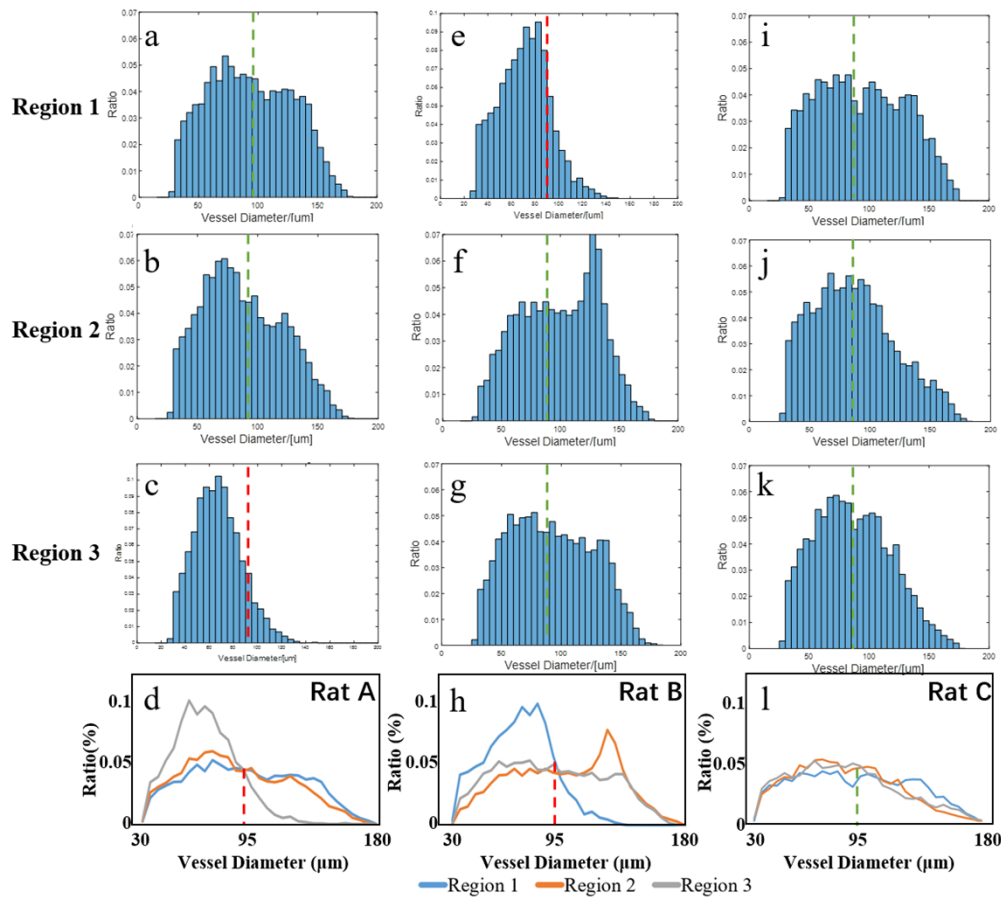
Fig. 4. Quantification on distribution ratios of vessel diameter in the regions marked by dashed boxes in Fig. 3. Red and green dash lines mark the intersection point of curves. (a – c, e – g, i – k) Vessel dimension distribution in the selected regions, respectively. (d, h, l) Combined data of the three regions in one rat.

which the vessels were continuous with high signal amplitude. Some shadows found in the PA MAP images (Figs. 3(a), (d) and (g)) were mainly caused by the unavoidable folded tissues.

Figures 3(b), (e), and (h) are the anatomical photos of rectum excised from the experimental rats. Black dashed boxes indicate the imaging regions shown in Figs. 3(a), (d), and (g), respectively. Blue dotted lines indicate the position of the pathological section at the tumor-suspected regions. To verify the imaging results, pathological sectioning was conducted. Figures 3(c), (f), (i), (j), and (k) are the results of pathological section dealt by H&E staining. Red squares mark the enlarged regions. Red arrows highlight the details of neoplasia.

In Fig. 3(c), in the red square region, some crowded tumor cells (indicated by red arrow) were witnessed in the mucosa layer and identified as intraepithelial neoplasia. There is a dark area at the one o'clock direction, which was identified as lymphocytes. In Fig. 3(f), the thick and irregular glands are visualized in the hyperplastic submucosa layer. The crowded tumor nucleuses formed in a wide variety of shapes and sizes, shown in the enlarged figure. Some tumor cell invasion can be found on the muscularis propria layer (shown by red arrow), which was recognized as adenoma. Figure 3(k) shows the structure of a normal rectum, generally including three layers: mucosa, submucosa and muscularis propria. Most of the vessels distribute in the
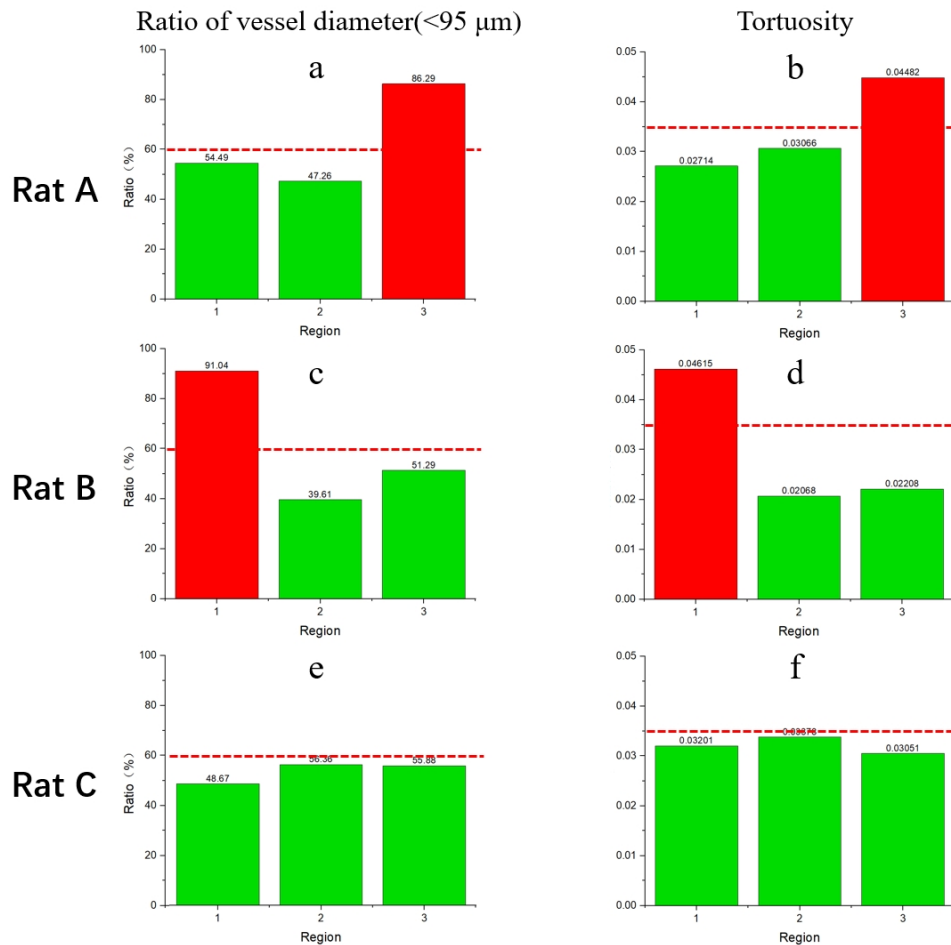
Fig. 5. Ratio of vessel diameter (<95 μm) and tortuosity of the labeled regions. Red color marks the tumor regions. Red dash lines indicate "thresholds" of tumor and normal data.

4. Discussion

submucosal layers, OR-PAE may show the potential for image pathological section morphology with high resolution in a less-trauma way, which is invaluable information for the early diagnosis of tumor development. However, this technology in Fig. 3(g) yet the pathological finding was verified by pathologist. requirement is more complicated requiring a large DOF, which is contradictory to high-resolution imaging. Here, we designed an OR-PAE catheter, showing a high PA resolution of 3.3 μm. For the first time, a systematic work on tumor study using OR-PAE was completed including the development of catheter with proper resolution and DOF, animal model experiment, *in-vivo* imaging, and data quantification.

It is important to note that during the late stage of modeling, the rat rectal tumor may trigger occurrences of watery stools or mucosal bleeding, potentially contaminating the endoscopic catheter during imaging and resulting in artifacts. Thus, caution must be exercised when repeatedly flushing to avoid harming the vulnerable rectal mucosa. Besides, the rats were observed to be emaciated and weak due to the terminal tumor, rendering them more susceptible to mortality under anesthesia during imaging experiments, thereby causing further difficulty to this study. The optimal imaging window should be within the early stages of modeling, preferably within four months.

3.7. Quantification of the vessel network

Figure 4 shows the vessel dimension distribution of selected regions in Fig. 3 shown by bar diagrams, suggesting that diameter of vessels was ranging from ~20 μm to 180 μm. The dash line marks the intersection point of the curves, which means the vessel distribution was divided into big and micro vessels at 95 μm. The red dash line highlights the tumor region, while the green dash line indicates the normal region.

Figure 5 clearly illustrates the statistical results of diameter and tortuosity in quantification. Figures 5(a), (c), and (e) are the diameter quantification results of the micro vessels (<95 μm). Figures 5(b), (d), and (f) are the calculated tortuosity of the vessel curve based on the quantification. The ratios of micro vessels amount in tumor regions were 86.29% (in Fig. 5(a)) and 91.04% (in Fig. 5(c)), respectively, while the ratios of micro vessels amount were under 60% in the normal

regions. The quantification data of tortuosity showed the similar trend. The tumor-suspected regions reached a high tortuosity with a ratio of >0.045%, while the tortuosity in the normal regions was below the ratio of 0.035%.

4. Discussion

In recent years, OR-PAE has shown the potential on imaging the vascular morphology with high resolution in the GI tract, which is invaluable information for early diagnosis of tumor development. However, this technology has not yet been validated on *in vivo* GI tumors. The tumor environment is more complicated requiring a large DOF, which is contradictory to high-resolution imaging. Here, we designed an OR-PAE catheter, showing a high PA resolution of 27 µm and a matched DOF of ~400 µm. For the first time, a systematic work on tumor study using OR-PAE was completed including the development of catheter with proper resolution and DOF, animal model experiment, *in-vivo* imaging, and data quantification.

It is important to note that during the late stage of modeling, the rat rectal tumor may trigger occurrences of watery stools or mucosal bleeding, potentially contaminating the endoscopic catheter during imaging and resulting in artifacts. Thus, caution must be exercised when repeatedly flushing to avoid harming the vulnerable rectal mucosa. Besides, the rats were observed to be emaciated and weak due to the terminal tumor, rendering them more susceptible to mortality under anesthesia during imaging experiments, thereby causing further difficulty to this study. The optimal imaging window should be within the early stages of modeling, preferably within four months.

Most of the vessels distribute in the submucosa layer of the rectum. The pathological analysis of the rat rectum was performed before the imaging experiments, and the results showed the thickness of submucosa layer was ~400 um, as shown in Fig. 3(k). To adapt the imaging range, the diameter of the laser spot was designed to be ~18.5 µm (see Supplement 1) from the depth of 1.3 mm to 1.7 mm, capable of imaging the vessels in the mucosa and submucosa layers. In Fig. 2(a), most of the PA signals distribute between the depth of 1.3 mm and 1.7 mm. In Figs. 2(b) and (d), the B-scan images verified that the vessels mainly distribute within the depth range of 400 um, which is consistent with the physiological results. It is noticeable that although the disease brought great complexity to the GI environment, such as the irregularity of the tract and thicken submucosa, the vasculature of tumor-suspected regions was still clearly imaged as shown in Figs. 2, 3(a), (d), and (g). All the results suggest that the proposed catheter is capable of conducting *in-vivo* GI tumor imaging in animal model, providing integrated vasculature of GI tract.

In this study, a critical question would be raised on how to identify the disease based on the vasculature of the tract from the PA images. In general, the PA images could tell the differences as angiogenesis of tumors shows very specific characteristics from the normal vessels. Nevertheless, the visual inspection may not be very reliable to identify the tumors from all the tumor-suspected regions. Figure 3 shows the imaging and pathological results obtained from three animal models, in which the tumor-suspected regions were judged visually from the PA imaging results. On the other hand, pathological sections proved that only two regions were neoplasia, suggesting that the visual inspection is not good enough to recognize the tumor regions. It is necessary to develop a method to objectively define the "tumor region". Thus, some algorithms are used to quantify the characteristics of vasculature morphology including the vessel diameter and the tortuosity, which are both important for featuring the tumor vessels [20–24].

The aforementioned quantification results were calculated through morphological analysis. Specifically, metrics of vascular diameter and curvature were applied to distinguish between tumor and normal regions in the vessel images. Additional metrics, such as intensity level changes, vascular density, and vessel complexity, can also be utilized for the tumor differentiation. In this pilot study, our current approach used two metrics to identify tumor and normal regions,

but it is not an ultimate solution. Tumors are various in GI tract. Only two metrics are not sufficient to characterize all types of tumors. Future studies should consider the incorporation of multiple metrics to feature different tumors. The inclusion of a broader range of metrics in the quantification process would enhance the accurate of the results. Future work will involve the incorporation of additional metrics for a more comprehensive analysis.

Oxygen saturation (sO_2) is an additional important parameter for featuring tumor vessels and environment, offering insights into total hemoglobin concentration and providing other valuable functional information. Previous studies have successfully imaged the sO_2 of normal rectal vessels. However, tumor vessels in the early stages exhibit smaller and deeper characteristics compared to normal vessels. This necessitates high resolution and a long imaging depth-of-field, which are the highlights of this work. There is one single wavelength in our system. To image sO_2 of rectal tumors, the original system of the OR-PAE should be redesigned. We propose to fabricate a dual-wavelength-laser system specifically designed to acquire photoacoustic images of rectal tumor vessels, enabling calculation of their sO_2.

The analysis results in Fig. 4 show that more micro vessels ($<95\,\mu m$) are distributed in the tumor-suspected regions except Region 1 in Rat C, while more big vessels ($>95\,\mu m$) are distributed in the normal regions. We set $95\,\mu m$ as a cut-off point because all the curves had a common intersection at $\sim 95\,\mu m$ when all the data overlapped together, as shown in Figs. 4(d), (h), and (l). To further analyze the quantification results, the amount ratios of micro vessels ($<95\,\mu m$) and the vessel tortuosity were calculated and shown in Fig. 5.

It was found that the vasculatures of tumor regions of Rats A and B exhibited more micro vessels (86.29% and 91.04%, respectively) and higher tortuosity (0.045 and 0.046, respectively). For the tumor-suspected region in Rat C, the calculated amount ratios of micro vessels and tortuosity did not show obvious differences from those in the normal regions. After imaging, pathological and quantitative analysis was conducted to determine the tumor and normal regions. And then, the maximum value of quantification result was confirmed from all the normal regions, which were the statistical results bases on the current data. The "threshold" was set a little higher than the maximum values in order to better differentiate the tumor from all the regions, which is not an optimal value based on such a small sampling size. The true threshold should be refined by analyzing a large number of sampling regions in the future work.

Though the results show the potential of the proposed OR-PAE catheter, there remains rooms to further improve the performance. First, the improvement could lie in adopting a PMN-PT based ultrasound transducer, known for its higher detection sensitivity. This enhancement could enable a reduction in laser fluence (~ 70 mJ/cm^2 in this work), thereby enhancing the overall performance of catheter. Second, continuous *in-vivo* OR-PAE imaging would be conducted from the early period of the modeling. The tumor development can be monitored under the longitudinal observation. Third, imaging catheters with further larger DOF and higher imaging resolution would be desired to better adapt the diameter of the growing rat rectum in different periods. Fourth, a dual-wavelength-laser system would be fabricated to acquire the photoacoustic images of rectal vessel, which can be designed to acquire photoacoustic images of rectal tumor vessels, enabling calculation of their sO_2. Finally, experiments of diagnosis and treatment on rectal tumors would be conducted for studying the effects of drugs on tumors.

5. Conclusion

In summary, for the first time, OR-PAE imaging was conducted on rectal tumors *in vivo*, showing the vascular network morphology of the tumor and normal regions of different rat rectums. An OR-PAE catheter was designed with a high resolution of $\sim 27\,\mu m$ and a matched DOF of $\sim 400\,\mu m$, capable of imaging the vessels up to the submucosa layer. Based on the quantitative analysis of tumor-suspected regions and normal regions in the PA images, the tumor regions could be verified by comparing the blood vessel diameter and tortuosity, which was consistent with the

pathological section. All the imaging and quantification results show that the OR-PAE has great application potential in tumor diagnosis, evaluation and monitoring of therapeutic efficacy.

Disclosures. The authors declare that there are no conflicts of interest related to this article.

Data Availability. Data underlying the results presented in this paper are not publicly available at this time but may be obtained from the authors upon reasonable request.

Supplemental document. See Supplement 1 for supporting content.

References

1. A. Link, G. Treiber, B. Peters, *et al.*, "Impact of Endoscopy-Based Research on Quality of Life in Healthy Volunteers," World J Gastroenterol **16**(4), 467–473 (2010).
2. W. Du, T. L. Frankel, M. Green, *et al.*, "Ifngamma Signaling Integrity in Colorectal Cancer Immunity and Immunotherapy," Cell. Mol. Immunol. **19**(1), 23–32 (2022).
3. E. T. Cârțână, D. I. Gheonea, and A. Săftoiu, "Advances in Endoscopic Ultrasound Imaging of Colorectal Diseases," World J Gastroenterol **22**(5), 1756–1766 (2016).
4. L. Y. Chen, L. Wang, Y. X. Ren, *et al.*, "The Circular Rna Circ-Erbin Promotes Growth and Metastasis of Colorectal Cancer by Mir-125a-5p and Mir-138-5p/4ebp-1 Mediated Cap-Independent Hif-1α Translation," Mol. Cancer **19**(1), 164 (2020).
5. J. M. Yang, C. Li, R. Chen, *et al.*, "Optical-Resolution Photoacoustic Endomicroscopy in Vivo," Biomed. Opt. Express **6**(3), 918–932 (2015).
6. K. D. Xiong, S. H. Yang, X. W. Li, *et al.*, "Autofocusing Optical-Resolution Photoacoustic Endoscopy," Opt. Lett. **43**(8), 1846–1849 (2018).
7. X. W. Li, K. D. Xiong, and S. H. Yang, "Large-Depth-of-Field Optical-Resolution Colorectal Photoacoustic Endoscope," Appl. Phys. Lett. **114**(16), 1 (2019).
8. K. Xiong, W. Wang, T. Guo, *et al.*, "Shape-Adapting Panoramic Photoacoustic Endomicroscopy," Opt. Lett. **44**(11), 2681–2684 (2019).
9. H. Sun, W. Wang, Z. X. Zhang, *et al.*, "Real-Time Optical-Resolution Photoacoustic Endoscope," Appl. Phys. Express **14**(4), 042012 (2021).
10. L. Wang, P. Lei, X. Wen, *et al.*, "Tapered Fiber-Based Intravascular Photoacoustic Endoscopy for High-Resolution and Deep-Penetration Imaging of Lipid-Rich Plaque," Opt. Express **27**(9), 12832–12840 (2019).
11. X. Wen, P. Lei, S. Huang, *et al.*, "High-Fluence Relay-Based Disposable Photoacoustic-Ultrasonic Endoscopy for *in Vivo* Anatomical Imaging of Gastrointestinal Tract," Photonics Res. **11**(1), 55–64 (2023).
12. Z. D. Guo, Y. Li, and S. L. Chen, "Miniature Probe for *in Vivo* Optical- and Acoustic-Resolution Photoacoustic Microscopy," Opt. Lett. **43**(5), 1119–1122 (2018).
13. H. Guo, C. L. Song, H. K. Xie, *et al.*, "Photoacoustic Endomicroscopy Based on a Mems Scanning Mirror," Opt. Lett. **42**(22), 4615–4618 (2017).
14. M. Kim, K. W. Lee, K. Kim, *et al.*, "Optical-Resolution Photoacoustic and Ultrasonic Mini-Probe System for Gastrointestinal Endoscopy," Photoacoustics **26**, 100346 (2022).
15. K. Watanabe, B. S. Reddy, J. H. Weisburger, *et al.*, "Effect of Dietary Alfalfa, Pectin, and Wheat Bran on Azoxymethane-or Methylnitrosourea-Induced Colon Carcinogenesis in F344 Rats," J Natl Cancer Inst **63**(1), 141–145 (1979).
16. K. Venkatachalam, R. Vinayagam, M. Arokia Vijaya Anand, *et al.*, "Biochemical and Molecular Aspects of 1,2-Dimethylhydrazine (Dmh)-Induced Colon Carcinogenesis: A Review," Toxicol. Res. **9**(1), 2–18 (2020).
17. Z. Huang, C. A. Liu, P. Z. Cai, *et al.*, "Omega-3pufa Attenuates Mnu-Induced Colorectal Cancer in Rats by Blocking Pi3 k/Akt/Bcl-2 Signaling," OncoTargets Ther. **13**, 1953–1965 (2020).
18. D. Chandel, M. Sharma, V. Chawla, *et al.*, "Characterization and Identification of Antigenotoxic and Anticancerous Indigenous Probiotics and Their Prophylactic Potential in Experimental Colon Carcinogenesis," Sci. Rep. **9**(1), 14769 (2019).

19. Y. Li, R. Lin, C. Liu, *et al.*, "*In Vivo* Photoacoustic/Ultrasonic Dual-Modality Endoscopy with a Miniaturized Full Field-of-View Catheter," J Biophotonics **11**(10), e201800034 (2018).

20. M. Sun, C. Li, N. Chen, *et al.*, "Full Three-Dimensional Segmentation and Quantification of Tumor Vessels for Photoacoustic Images," Photoacoustics **20**, 100212 (2020).

21. Q. Zhao, R. Q. Lin, C. B. Liu, *et al.*, "Quantitative Analysis on *in Vivo* Tumor-Microvascular Images from Optical-Resolution Photoacoustic Microscopy," J. Biophotonics **12**(6), e201800421 (2019).

22. E. Bullitt, G. Gerig, S. M. Pizer, *et al.*, "Measuring Tortuosity of the Intracerebral Vasculature from Mra Images," IEEE Trans. Med. Imaging **22**(9), 1163–1171 (2003).

23. L. Vincent, "Morphological Grayscale Reconstruction in Image Analysis: Applications and Efficient Algorithms," IEEE Trans. on Image Process. **2**(2), 176–201 (1993).

24. T. D. Le, S.-Y. Kwon, and C. Lee, "Segmentation and Quantitative Analysis of Photoacoustic Imaging: A Review," Photonics **9**(3), 176 (2022).